

# Efficient and fully-automatic retinal choroid segmentation in OCT through DL-based distillation of a hand-crafted pipeline

Jamie Burke<sup>\*1</sup>, Justin Engelmann<sup>\*2,3</sup>, Charlene Hamid<sup>4</sup>, Megan Reid-Schachter<sup>4</sup>, Tom Pearson<sup>5</sup>, Dan Pugh<sup>6</sup>, Neeraj Dhaun<sup>6</sup>, Stuart King<sup>1</sup>, Tom MacGillivray<sup>4,7</sup>, Miguel O. Bernabeu<sup>2,3,8</sup>, Amos Storkey<sup>2</sup> and Ian J.C. MacCormick<sup>9,10</sup>

<sup>1</sup> School of Mathematics, University of Edinburgh  
jamie.burke@ed.ac.uk

<sup>2</sup> School of Informatics, University of Edinburgh  
justin.engelmann@ed.ac.uk

<sup>3</sup> Centre for Medical Informatics, University of Edinburgh

<sup>4</sup> Edinburgh Clinical Research Facility and Imaging, University of Edinburgh

<sup>5</sup> University Hospital Wales, NHS Wales

<sup>6</sup> British Heart Foundation Centre for Cardiovascular Science, University of Edinburgh

<sup>7</sup> Centre for Clinical Brain Sciences, University of Edinburgh

<sup>8</sup> The Bayes Centre, University of Edinburgh

<sup>9</sup> Centre for Inflammation Research, University of Edinburgh

<sup>10</sup> Institute for Adaptive and Neural Computation, University of Edinburgh

**Abstract.** Retinal vascular phenotypes, derived from low-cost, non-invasive retinal imaging, have been linked to systemic conditions such as cardio-, neuro- and reno-vascular disease. Recent high-resolution optical coherence tomography (OCT) allows imaging of the choroidal microvasculature which could provide more information about vascular health that complements the superficial retinal vessels, which current vascular phenotypes are based on. Segmentation of the choroid in OCT is a key step in quantifying choroidal parameters like thickness and area. Gaussian Process Edge Tracing (GPET) is a promising, clinically validated method for this. However, GPET is semi-automatic and thus requires time-consuming manual interventions by specifically trained personnel which introduces subjectivity and limits the potential for analysing larger datasets or deploying GPET into clinical practice. We introduce DeepGPET, which distils GPET into a neural network to yield a fully-automatic and efficient choroidal segmentation method. DeepGPET achieves excellent agreement with GPET on data from 3 clinical studies (AUC=0.9994, Dice=0.9664; Pearson correlation of 0.8908 for choroidal thickness and 0.9082 for choroidal area), while reducing the mean processing time per image from 34.49s ( $\pm 15.09$ ) to 1.25s ( $\pm 0.10$ ) on a standard laptop CPU and removing all manual interventions. DeepGPET will be made available for researchers upon publication.

**Keywords:** Segmentation · Choroid · Deep learning · OCT

\* Equal contribution.

## 1 Introduction

The retinal choroid is a complex, extensively interconnected vessel network positioned between the retina and the sclera. The choroid holds the majority of the vasculature in the eye and plays a pivotal role in nourishing the retina. Optical coherence tomography (OCT) is an ocular imaging modality that uses low-coherence light to construct a three-dimensional map of chorioretinal structures at the back of the eye. Standard OCT imaging does not visualise the deeper choroidal tissue well as it sits beneath the hyperreflective retinal pigment epithelium layer of the retina. Enhanced Depth Imaging OCT (EDI-OCT) overcomes this problem and offers improved visualisation of the choroid, thus providing a unique window into the microvascular network which not only resides closest to the brain embryologically, but also carries the highest volumetric flow per unit tissue weight compared to any other organ in the body. Since the advent of OCT, interest in the role played by the choroid in systemic health has been growing [28], as non-invasive imaging of the choroidal microvasculature may provide a novel location to detect systemic, microvascular changes early. Indeed, changes in choroidal blood flow, thickness and other markers have been shown to correspond with patient health such as choroidal thickness in chronic kidney disease [2] and choroidal area and vascularity in Alzheimer’s dementia [22].

Quantification of the choroid in EDI-OCT imaging requires segmentation of the choroidal space. However, this is a harder problem than retinal layer segmentation due to poor signal penetration from the device — and thus lower signal-to-noise ratio — and shadows cast by superficial retinal vessels and choroidal stroma tissue. This results in poor intra- and inter-rater agreement even with manual segmentation by experienced clinicians, and manual segmentation is too labour intensive and subjective to be practical for analysing large scale datasets. Semi-automated algorithms improve on this slightly but are typically multi-stage procedures, requiring traditional image processing techniques to prepare the images for downstream segmentation [9]. Methods based on graph theory such as Dijkstra’s algorithm [18, 24] or graph cut [15], as well as on statistical techniques including level sets [26, 29], contour evolution [11], and Gaussian mixture models [7] have been proposed previously. Concurrently, deep learning (DL)-based approaches have emerged. [6] used a DL model for choroid layer segmentation, but with traditional contour tracing as a post-processing step. Other DL-based approaches, too, combine traditional image processing techniques as pre- or post-processing steps [1, 17, 27] whereas others are fully DL-based [5, 31], the latter of which is in a similar vein to the proposed method. More recently, DL has been used to distil existing semi-automatic traditional image processing pipelines into a fully-automatic method [10].

Gaussian Process Edge Tracing (GPET), based on Bayesian machine learning [3], is a particularly promising method for choroid layer segmentation that has been clinically and quantitatively validated [4]. Gaussian process (GP) regression is used to model the upper and lower boundaries of the choroid from OCT scans. For each boundary, a recursive Bayesian scheme is employed to iteratively detect

Table 1: Overview of population characteristics. EDI: enhanced depth imaging.

	OCTANE	i-Test	Normative	Total
Subjects	47	5	30	82
Male/Female	24 / 23	0 / 5	20 / 10	44 / 38
Right/Left eyes	47 / 0	5 / 5	30 / 28	82 / 33
Age (Mean (SD))	48.8 (12.9)	34.4 (3.4)	49.1 (7.0)	48.0 (11.2)
Machine	Standard	FLEX	Standard	
Horizontal/Vertical	166 / 0	16 / 16	57 / 54	239 / 70
Volume	174	186	46	406
Total scans	340	218	157	715

boundary pixels based on the image gradient and the GP regressor’s distribution of candidate boundaries.

We aim to distil GPET into a fully-automatic method, DeepGPET, for choroidal segmentation that can process images without manual intervention in a fraction of the time — permitting analysis of large scale datasets and potential deployment into clinical care and research practice without prior training.

## 2 Methods

### 2.1 Data: Study populations and imaging devices

We used 715 OCT images belonging to 82 subjects from three studies: **OCTANE** [8], a study looking at renal function and impairment in chronic kidney disease patients. **i-Test**, a study recruiting pregnant women of any gestation or those who have delivered a baby within 6 months, including controls and individuals at high risk of complications. **Normative**, data from 30 healthy volunteers as a control group [20]. All studies conformed with the Declaration of Helsinki and received relevant ethical approval and informed consent from all subjects. Table 1 provides an overview of basic population characteristics and number of subjects/images of these studies.

Two Heidelberg spectral domain OCT SPECTRALIS devices were used for image acquisition: the Standard Module (OCT1 system) and FLEX Module (OCT2 system). The FLEX is a portable version that enables imaging of patients in a ward environment. Both machines imaged a 30° (8.7 mm) region, generating a macular, cross-sectional OCT B-scan at 768 × 768 pixel resolution. Notably, 14% of the OCT B-scans were non-EDI and thus present more challenging images with lower signal-to-noise ratio in the choroidal part of the OCT.

We split the data into training (603 images, 64 subjects), validation (58 images, 9 subjects) and test sets (54 images, 7 subjects) at the patient-level, stratified on scan types (EDI/non-EDI), cohorts, and image quality.

## 2.2 DeepGPET

Our approach is to distil GPET into a DL model to obtain an efficient and fully-automatic method. We fine-tune a UNet [23] with MobileNetV3 [13] backbone pre-trained on ImageNet for 60 epochs with batch size 16 using AdamW [16] ( $\text{lr} = 10^{-3}$ ,  $\beta_1 = 0.9$ ,  $\beta_2 = 0.999$ , weight decay =  $10^{-2}$ ). After epoch 30, we maintain an exponential moving average (EMA) of model weights which we then use as our final model. We use the following data augmentations: brightness and contrast changes, horizontal flipping, and simulated OCT speckle noise by applying Gaussian noise followed by multiplicative noise (all  $p = 0.5$ ); Gaussian blur and random affine transforms (both  $p = 0.25$ ). To reduce memory-load, we crop the black space above and below the OCT B-scan and process images at a resolution of  $544 \times 768$  pixels. Images are standardised by subtracting 0.1 and dividing by 0.2, and no further pre-processing is done. We used Python 3.11, PyTorch 2.0, Segmentation Models PyTorch [14] and the timm library [30]. Our code is available here [to be added upon publication].

## 2.3 Evaluation and statistical analysis

We used Dice coefficient and Area Under the ROC Curve (AUC) for evaluating agreement in segmentations, as well as the Pearson correlation  $r$  and Mean Absolute Error (MAE) for segmentation-derived choroid thickness and area. The calculation of thickness and area from the segmentation is described in more detail in [4]. Briefly, for thickness the average of 3 measures is used, taken at the fovea and 2,000 microns from it in either direction by drawing a perpendicular line from the upper boundary to the lower boundary to account for choroidal curvature. For area, pixels are counted in a region of interest 3,000 microns around the fovea, which corresponds to the commonly used Early Treatment Diabetic Retinopathy Study (ETDRS) macular area of  $6,000 \times 6,000$  microns [12].

We compare DeepGPET’s agreement with GPET’s segmentations against the repeatability of GPET itself. The creator of GPET, J.B., made both the original and repeated segmentations with GPET. Since both segmentations were done by the same person there is no inter-rater subjectivity at play here. Thus, the intra-rater agreement measured here is a best case scenario and forms an upper-bound for agreement with the original segmentation.

In addition to quantitative evaluations, we also compared segmentations by GPET and DeepGPET for 20 test set OCT images qualitatively by having them rated by I.M., an experienced clinical ophthalmologist. We selected 7 examples with the highest disagreement in thickness and area, 6 examples with disagreement closest to the median, and 7 examples with the lowest disagreement. Thus, these 20 examples cover cases where both methods are very different, cases of typical disagreement, and cases where both methods are very similar. In each instance, I.M. was blinded to which method produced which segmentation, and was asked to rate each one along three dimensions: Quality of the upper boundary, the lower boundary and overall smoothness using an ordinal scale: “Very bad”, “Bad”, “Okay”, “Good”, “Very good”.

Table 2: Metrics for DeepGPET and repeated GPET using the initial GPET annotation as “ground-truth”. Time given as mean  $\pm$  standard deviation.

Method	AUC	Dice	Time (s/img)	Thickness		Area	
				Pearson $r$	MAE ( $\mu\text{m}$ )	Pearson $r$	MAE ( $\text{mm}^2$ )
DeepGPET	0.9994	0.9664	1.25 $\pm$ 0.10	0.8908	13.3086	0.9082	0.0699
Repeat GPET	0.9812	0.9672	34.49 $\pm$ 15.09	0.9527	10.4074	0.9726	0.0486

### 3 Results

#### 3.1 Quantitative

Table 2 shows the results for DeepGPET and repeat GPET, compared to the initial GPET segmentations as “ground-truth”.

**Agreement in segmentation.** Both methods have excellent agreement with the original segmentations. DeepGPET’s agreement is comparable to the repeatability of GPET itself, with DeepGPET having a slightly higher AUC (0.9994 vs 0.9812) and slightly lower Dice coefficient (0.9664 vs 0.9672). DeepGPET having a higher AUC but lower Dice suggests that for pixels where it disagrees with GPET after thresholding the confidence is lower than for ones where it agrees with GPET and so the raw DeepGPET probabilities provide a reasonable measure of uncertainty.

**Processing speed and manual interventions.** Both methods were compared on the same standard laptop CPU. DeepGPET processed the images in only 3.6% of the time that GPET needed. DeepGPET ran fully-automatic and successfully segmented all images, whereas GPET required 1.27 manual interventions on average, including selecting initial pixels and manual adjustment of GPET parameters when the initial segmentation failed.

This results in massive time savings: A standard OCT volume scan consists of 61 B-scans. With GPET, processing such a volume for a single eye takes about 35 minutes during which a person has to select initial pixels to guide tracing (for all images) and adjust parameters if GPET initially failed (for about 25% of images). In contrast, DeepGPET could do the same processing in about 76 seconds on the same hardware, during which no manual input is needed. DeepGPET could even be GPU-accelerated to cut the processing time by another order of magnitude.

The lack of manual interventions required by DeepGPET means that no subjectivity is introduced unlike GPET, particularly when used by different people. Additionally, DeepGPET does not require specifically trained analysts and could be used fully-automatically in clinical practice.

**Agreement in choroid area and thickness.** GPET showed very high repeatability for thickness (Pearson  $r=0.9527$ , MAE=10.4074  $\mu\text{m}$ ) and area (Pearson

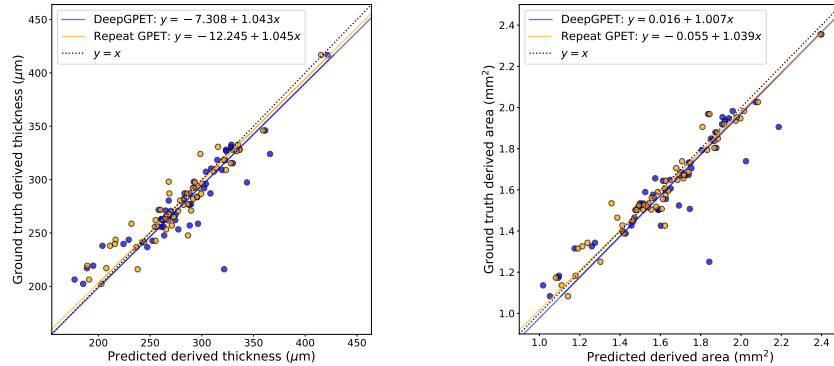


Fig. 1: Correlation plots comparing derived measures of mean choroid thickness (a) and choroid area (b) using DeepGPET and the re-segmentations using GPET.

$r=0.9726$ ,  $\text{MAE}=0.0486 \text{ mm}^2$ ). DeepGPET achieved slightly lower, yet also very high agreement for both thickness (Pearson  $r=0.8908$ ,  $\text{MAE}=13.3086 \mu\text{m}$ ) and area (Pearson  $r=0.9082$ ,  $\text{MAE}=0.0699 \text{ mm}^2$ ). Fig. 1 shows correlation plots for thickness and area. DeepGPET’s agreement with GPET does not quite reach the repeatability of GPET itself, when used by the same experienced analyst, but it is quite comparable and high in absolute terms. Especially noteworthy is that the MAE for thickness and area is only 21% lower for thickness and 30% lower for area for repeated GPET than for DeepGPET, thus DeepGPET comes quite close to optimal performance, i.e. best case repeatability where the same experienced analyst did both sets of annotation.

Furthermore, the regression fits in both derived measures for DeepGPET are closer to the identity line than for the repeated GPET measurements. For thickness, the linear fit estimated a slope value of 1.043 (95% confidence interval of 0.895 to 1.192) and intercept of  $-7.308 \mu\text{m}$  (95% confidence interval of  $-48.967 \mu\text{m}$  to  $34.350 \mu\text{m}$ ). For area, the linear fit estimated a slope value of 1.01 (95% confidence interval of 0.878 to 1.137) and an intercept of  $0.016 \text{ mm}^2$  (95% confidence interval of  $-0.195 \text{ mm}^2$  to  $0.226 \text{ mm}^2$ ). All confidence intervals contain 1 and 0 for the slope and intercepts, respectively, suggesting no systematic bias or proportional difference between GPET and DeepGPET [19, 21].

### 3.2 Qualitative

Table 3 shows the results of the adjudication between DeepGPET and GPET itself for the 20 test set OCT images. The upper boundary was rated as “Very good” for both methods in all 20 cases. However, for the lower boundary, DeepGPET was rated as “Bad” in 2 cases for the lower boundary and 1 case for smoothness. Otherwise, both methods performed very similarly.

Fig. 2 shows some examples. In (a), DeepGPET segments more of the temporal region than GPET does, providing a full width segmentation which was preferred by the rater. Additionally, both approaches are able to segment a

Table 3: Qualitative ratings of 20 test set segmentations along 3 key dimensions. The rater was blinded to the identity of the methods and their order was randomised for every example.

Method	Upper boundary	Lower boundary	Smoothness
DeepGPET	Very good: 20	Very good: 4, Good: 10, Okay: 4, Bad: 2	Very good: 5, Good: 12, Okay: 2, Bad: 1
GPET	Very good: 20	Very good: 6, Good: 6, Okay: 8, Bad: 0	Very good: 6, Good: 13, Okay: 1, Bad: 0

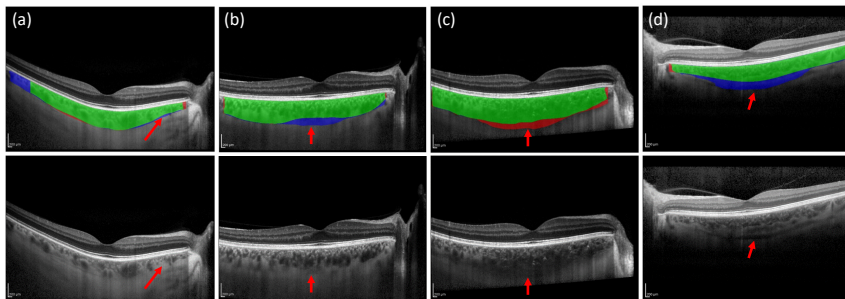


Fig. 2: Four examples from the adjudication. The rater preferred DeepGPET for (a–b) and GPET for (c–d). Top row: green, segmented by both GPET and DeepGPET; red, GPET only; and blue, DeepGPET only. Bottom row: arrows indicate important choroidal features which can make segmentation challenging. (a): no large vessels in nasal region to guide segmentation; (b): lower boundary very faint and below the posterior most vessels; (c): lower boundary noisy and faint; (d): large suprachoroidal space visible.

smooth boundary, even in regions with stroma fluid obscuring the lower boundary (red arrow). In (b), the lower boundary for this choroid is very faint and is actually below the majority of the vessels sitting most posterior (red arrow). DeepGPET produced a smooth and concave boundary preferred by the rater, while GPET fell victim to hugging the posterior most vessels in the subfoveal region. In (c), DeepGPET rejected the true boundary in the low contrast region (red arrow) and opted for a more well-defined one, while GPET segmented the more uncertain path. Since GPET permits human intervention, there is more opportunity to fine tune it’s parameters to fit what the analyst believes is the true boundary. Here, the rater preferred GPET, while DeepGPET’s under-confidence led to under-segmentation, and ultimately to a bad rating. In (d) — the test image with the largest disagreement in thickness and area — the lower boundary is difficult to delineate due to a thick suprachoroidal space (red arrow) and thus a lack of lower boundary definition. Here, the rater gave a bad rating to DeepGPET and preferred GPET, while remarking that GPET actually under-segmented the choroid by intersecting through posterior vessels.

## 4 Discussion

We developed DeepGPET, a fully-automatic and efficient method for choroid layer segmentation, by distilling GPET, a clinically validated semi-automatic method. DeepGPET achieved excellent agreement with GPET on held-out data in terms of segmentation and derived choroidal metrics, approaching the repeatability of GPET itself. Most importantly, DeepGPET does not require specialist training and can process images fully-automatically in a fraction of the time, enabling analysis of large scale datasets and potential deployment in clinical practice.

While the observed agreement was very high, it was not perfect. However, even higher agreement with GPET would not necessarily produce a better method as GPET itself is not perfect. Conceptually, there is debate around the exact location of choroid-scleral interface (CSI), i.e. the lower choroid boundary in OCT images. CSI is commonly defined, e.g. by the original authors behind EDI-OCT [25], as the smooth inner boundary between the choroid and sclera, or just below the most posterior vessels but excluding the suprachoroidal space. However, even that definition is still debated and can be hard to discern in practice. Not all choroids are smooth, and there are edge cases like vessels passing from the sclera into the choroid, or stroma fluid obscurations that make the boundary even more ambiguous.

For quantitative analysis of choroidal phenotypes, the specific definition of the CSI is secondary to applying the same, consistent definition across and within patients. Here, fully-automatic methods like DeepGPET provide a large benefit by removing the subjectivity present in semi-automatic methods. In GPET, the initial points being selected determine what edge is being traced as the CSI, and thus two analysts with different understandings could produce vastly different segmentations. With DeepGPET, the same image is always segmented in the same way, removing subjectivity.

In the present work, we used data from three studies, two OCT devices and included both EDI and non-EDI scans. However, we only used data from subjects that were either healthy or had systemic but not eye disease, to which DeepGPET might not be robust to. In future work, we plan to externally validate DeepGPET and include cases of ocular pathologies. A further limitation is that while GPET has been clinically validated, not all segmentations used for training DeepGPET were entirely perfect. Thus, revisiting some of the existing segmentations and manually improving them to a “gold standard” for purposes of training the model could improve DeepGPET. For instance, GPET does not always segment the whole width of the choroid. Interestingly, DeepGPET already is able to do that in some cases (e.g. Fig. 2(a)), but also does emulate the incomplete segmentations by GPET in other cases. A model trained on enhanced “gold standard” segmentations would produce even better segmentations.

Finally, we have focused on segmentation as it is the most important and most time-consuming step of choroidal analysis. However, the location of the fovea on OCT images needs identified to define the region of interest for derived measurements such as thickness, area and volume. Identifying the fovea is less time-consuming or ambiguous than choroid segmentation, and so we plan to



extend DeepGPET to output the fovea location. This would make DeepGPET a fast and efficient end-to-end framework capable of converting a raw OCT image to a set of clinically meaningful segmentation-derived measurements. Likewise, segmenting the choroidal vessels is a very challenging task even for humans and would be prohibitively time-consuming to do manually, but in the future we aim to explore whether DeepGPET can automatically segment the vasculature within the choroid as well.

## Acknowledgements

This work was supported by the Medical Research Council (grant MR/N013166/1) and the UKRI Centre (grant EP/S02431X/1), as part of the Precision Medicine DTP and Biomedical AI CDT with the University of Edinburgh, respectively. For the purpose of open access, the authors have applied a creative commons attribution (CC BY) licence to any author accepted manuscript version arising. The authors would also like to thank all participants in the studies used in this paper, as well as all staff at the Edinburgh Imaging Facility who contributed to image acquisition for this study.

## References

1. Al-Bander, B., Williams, B.M., Al-Taei, M.A., Al-Nuaimy, W., Zheng, Y.: A novel choroid segmentation method for retinal diagnosis using deep learning. In: 2017 10th International Conference on Developments in eSystems Engineering (DeSE). pp. 182–187. IEEE (2017)
2. Balmforth, C., van Bragt, J.J., Ruijs, T., Cameron, J.R., Kimmitt, R., Moorhouse, R., Czopek, A., Hu, M.K., Gallacher, P.J., Dear, J.W., et al.: Chorioretinal thinning in chronic kidney disease links to inflammation and endothelial dysfunction. *JCI insight* **1**(20) (2016)
3. Burke, J., King, S.: Edge tracing using gaussian process regression. *IEEE Transactions on Image Processing* **31**, 138–148 (2021)
4. Burke, J., Pugh, D., Farrah, T., Hamid, C., Godden, E., MacGillivray, T., Dhaun, N., Baillie, K., King, S., MacCormick, I.J.C.: Evaluation of an automated choroid segmentation algorithm in a longitudinal kidney donor and recipient cohort (2023)
5. Chen, H.J., Huang, Y.L., Tse, S.L., Hsia, W.P., Hsiao, C.H., Wang, Y., Chang, C.J.: Application of artificial intelligence and deep learning for choroid segmentation in myopia. *Translational Vision Science & Technology* **11**(2), 38–38 (2022)
6. Chen, M., Wang, J., Oguz, I., VanderBeek, B.L., Gee, J.C.: Automated segmentation of the choroid in edi-oct images with retinal pathology using convolution neural networks. In: Fetal, Infant and Ophthalmic Medical Image Analysis: International Workshop, FIFI 2017, and 4th International Workshop, OMIA 2017, Held in Conjunction with MICCAI 2017, Québec City, QC, Canada, September 14, Proceedings 4. pp. 177–184. Springer (2017)
7. Danesh, H., Kafieh, R., Rabbani, H., Hajizadeh, F.: Segmentation of choroidal boundary in enhanced depth imaging octs using a multiresolution texture based modeling in graph cuts. *Computational and mathematical methods in medicine* **2014** (2014)

8. Dhaun, N.: Optical coherence tomography and nephropathy: The octane study. <https://clinicaltrials.gov/ct2/show/NCT02132741> (2014), clinicalTrials.gov identifier: NCT02132741. Updated November 4, 2022. Accessed May 31st, 2023
9. Eghtedar, R.A., Esmaceli, M., Peyman, A., Akhlaghi, M., Rasta, S.H.: An update on choroidal layer segmentation methods in optical coherence tomography images: a review. *Journal of Biomedical Physics & Engineering* **12**(1), 1 (2022)
10. Engelmann, J., Villaplana-Velasco, A., Storkey, A., Bernabeu, M.O.: Robust and efficient computation of retinal fractal dimension through deep approximation. In: *Ophthalmic Medical Image Analysis: 9th International Workshop, OMIA 2022, Held in Conjunction with MICCAI 2022, Singapore, Singapore, September 22, 2022, Proceedings*. pp. 84–93. Springer (2022)
11. George, N., Jiji, C.: Two stage contour evolution for automatic segmentation of choroid and cornea in oct images. *Biocybernetics and biomedical Engineering* **39**(3), 686–696 (2019)
12. Group, E.T.D.R.S.R., et al.: Early treatment diabetic retinopathy study design and baseline patient characteristics: Etdrs report number 7. *Ophthalmology* **98**(5), 741–756 (1991)
13. Howard, A., Sandler, M., Chu, G., Chen, L.C., Chen, B., Tan, M., Wang, W., Zhu, Y., Pang, R., Vasudevan, V., et al.: Searching for mobilenetv3. In: *Proceedings of the IEEE/CVF international conference on computer vision*. pp. 1314–1324 (2019)
14. Iakubovskii, P.: Segmentation models pytorch. [https://github.com/qubvel/segmentation\\_models\\_pytorch](https://github.com/qubvel/segmentation_models_pytorch) (2019)
15. Kajić, V., Esmacelpour, M., Považay, B., Marshall, D., Rosin, P.L., Drexler, W.: Automated choroidal segmentation of 1060 nm oct in healthy and pathologic eyes using a statistical model. *Biomedical optics express* **3**(1), 86–103 (2012)
16. Loshchilov, I., Hutter, F.: Decoupled weight decay regularization. arXiv preprint arXiv:1711.05101 (2017)
17. Masood, S., Fang, R., Li, P., Li, H., Sheng, B., Mathavan, A., Wang, X., Yang, P., Wu, Q., Qin, J., et al.: Automatic choroid layer segmentation from optical coherence tomography images using deep learning. *Scientific reports* **9**(1), 3058 (2019)
18. Masood, S., Sheng, B., Li, P., Shen, R., Fang, R., Wu, Q.: Automatic choroid layer segmentation using normalized graph cut. *IET Image Processing* **12**(1), 53–59 (2018)
19. Passing, H., Bablok, W.: A new biometrical procedure for testing the equality of measurements from two different analytical methods. application of linear regression procedures for method comparison studies in clinical chemistry, part i (1983)
20. Pearson, T., Chen, Y., Dhillon, B., Chandran, S., van Hemert, J., MacGillivray, T.: Multi-modal retinal scanning to measure retinal thickness and peripheral blood vessels in multiple sclerosis. *Scientific Reports* **12**(1), 20472 (2022)
21. Ranganathan, P., Pramesh, C., Aggarwal, R.: Common pitfalls in statistical analysis: Measures of agreement. *Perspectives in clinical research* **8**(4), 187 (2017)
22. Robbins, C.B., Grewal, D.S., Thompson, A.C., Powers, J.H., Soundararajan, S., Koo, H.Y., Yoon, S.P., Polascik, B.W., Liu, A., Agrawal, R., et al.: Choroidal structural analysis in alzheimer disease, mild cognitive impairment, and cognitively healthy controls. *American Journal of Ophthalmology* **223**, 359–367 (2021)
23. Ronneberger, O., Fischer, P., Brox, T.: U-net: Convolutional networks for biomedical image segmentation. In: *Medical Image Computing and Computer-Assisted Intervention–MICCAI 2015: 18th International Conference, Munich, Germany, October 5–9, 2015, Proceedings, Part III* 18. pp. 234–241. Springer (2015)

24. Salafian, B., Kafieh, R., Rashno, A., Pourazizi, M., Sadri, S.: Automatic segmentation of choroid layer in edi oct images using graph theory in neutrosophic space. arXiv preprint arXiv:1812.01989 (2018)
25. Spaide, R.F., Koizumi, H., Pozonni, M.C.: Enhanced depth imaging spectral-domain optical coherence tomography. *American journal of ophthalmology* **146**(4), 496–500 (2008)
26. Srinath, N., Patil, A., Kumar, V.K., Jana, S., Chhablani, J., Richhariya, A.: Automated detection of choroid boundary and vessels in optical coherence tomography images. In: 2014 36th Annual International Conference of the IEEE Engineering in Medicine and Biology Society. pp. 166–169. IEEE (2014)
27. Sui, X., Zheng, Y., Wei, B., Bi, H., Wu, J., Pan, X., Yin, Y., Zhang, S.: Choroid segmentation from optical coherence tomography with graph-edge weights learned from deep convolutional neural networks. *Neurocomputing* **237**, 332–341 (2017)
28. Tan, K.A., Gupta, P., Agarwal, A., Chhablani, J., Cheng, C.Y., Keane, P.A., Agrawal, R.: State of science: choroidal thickness and systemic health. *Survey of ophthalmology* **61**(5), 566–581 (2016)
29. Wang, C., Wang, Y.X., Li, Y.: Automatic choroidal layer segmentation using markov random field and level set method. *IEEE journal of biomedical and health informatics* **21**(6), 1694–1702 (2017)
30. Wightman, R.: Pytorch image models. <https://github.com/rwightman/pytorch-image-models> (2019). <https://doi.org/10.5281/zenodo.4414861>
31. Zheng, G., Jiang, Y., Shi, C., Miao, H., Yu, X., Wang, Y., Chen, S., Lin, Z., Wang, W., Lu, F., et al.: Deep learning algorithms to segment and quantify the choroidal thickness and vasculature in swept-source optical coherence tomography images. *Journal of Innovative Optical Health Sciences* **14**(01), 2140002 (2021)